

New limits on the local Lorentz invariance violation of gravity in the Standard-Model Extension with pulsars

Yiming Dong,^{1,2} Ziming Wang,^{1,2,*} and Lijing Shao^{2,3,†}

¹*Department of Astronomy, School of Physics, Peking University, Beijing 100871, China*

²*Kavli Institute for Astronomy and Astrophysics, Peking University, Beijing 100871, China*

³*National Astronomical Observatories, Chinese Academy of Sciences, Beijing 100012, China*
(Dated: March 15, 2024)

Lorentz Violation (LV) is posited as a possible relic effect of quantum gravity at low energy scales. The Standard-Model Extension provides an effective field-theoretic framework for examining possible deviations attributed to LV. With their high observational accuracy, pulsars serve as ideal laboratories for probing LV. In the presence of LV, both the spin precession of solitary pulsars and orbital dynamics of binary pulsars would undergo modifications. Observations of pulse profiles and times of arrival (TOAs) of pulses allow for an in-depth investigation of these effects, leading to the establishment of strict limits on LV coefficients. We revisit the project of limiting local LV with updated pulsar observations. We employ a new parameter estimation method and utilize state-of-the-art pulsar timing observation data and get new limits on 8 linear combinations of LV coefficients based on 25 tests from 12 different systems. Compared to previous limits from pulsars, precision has improved by a factor of two to three. Additionally, we explore prospects for further improvements from pulsars. Simulation results indicate that more observations of spin precession in solitary millisecond pulsars could significantly enhance the accuracy of spatial LV coefficients, potentially by three to four orders of magnitude. As observational data accumulate, pulsars are anticipated to increasingly contribute to the tests of LV.

I. INTRODUCTION

Over the past century, General Relativity (GR) has withstood numerous high-precision experimental tests with flying colors [1, 2]. Despite its remarkable successes, GR also confronts challenges from both theoretical and observational perspectives. On the theoretical front, although GR and Standard Model (SM) form the foundation of our understanding of nature, there is longstanding aspiration for a theory that can describe all phenomena consistently. On the observational side, attempts to explain abnormal gravitational phenomena at large scales and the expansive nature of the cosmos have led to the introduction of dark matter and dark energy, which present another potential challenge to GR [3, 4]. In context, it has led to a growing focus on constructing a final theory, known as quantum gravity. From the perspective of experimental detection, quantum gravity is believed to exhibit significant deviations from GR at the Planck energy scale. However, verifying gravity theories at such extreme scales remains a formidable task [5, 6]. A feasible strategy is to search for relic effects of quantum gravity at low energy scales, such as the Lorentz Violation (LV) [5–9]. In some candidate theories of quantum gravity like string theory, Lorentz invariance could spontaneously break [10, 11]. Detecting evidences of LV will offer insights into the essence of quantum gravity. In this context, experiments and tests that focus on LV have garnered immense significance [12, 13].

The Standard-Model Extension (SME) is an effective field theory framework that catalogues the operators of LV [9, 14–16]. In the SME framework, one can derive the observational manifestations of LV conveniently and systematically. The Lagrangian density in the SME contains both Lorentz invariant terms and Lorentz violating terms. A LV term contains a LV operator constructed from the contraction of a conventional tensor operator with a violating tensor coefficient, and can be cataloged with a specific mass dimension d [17, 18]. Terms with a higher d are considered to appear at higher energy scales, which means a higher order correction in general. In this study, we consider the minimal gravitational LV cases where the conventional field operators are constructed using the Riemann tensor, corresponding to the mass-dimension $d = 4$ [9]. The Lagrangian density can be written in terms of the trace-free components of Riemann tensor as,

$$\mathcal{L}_{LV}^{(4)} = \frac{1}{16\pi G} (-uR + s^{\mu\nu}R_{\mu\nu}^T + t^{\alpha\beta\gamma\delta}C_{\alpha\beta\gamma\delta}), \quad (1)$$

where $R_{\mu\nu}^T$ is the trace-free Ricci tensor, $C_{\alpha\beta\gamma\delta}$ is the Weyl conformal tensor, and u , $s^{\mu\nu}$, $t^{\alpha\beta\gamma\delta}$ are Lorentz-violating fields. It is worth noting that these Lorentz-violating fields are observer Lorentz invariant but particle Lorentz violating [16]. Under *passive* observer transformations, all fields and Lorentz-violating background fields transform. Under *active* particle transformations, the localized fields and particles transform but the Lorentz-violating background fields remain fixed. $\mathcal{L}_{LV}^{(4)}$ changes under particle transformations so LV happens [9]. The Lorentz-violating fields u , $s^{\mu\nu}$, $t^{\alpha\beta\gamma\delta}$ can be divided into their vacuum expectation values \bar{u} , $\bar{s}^{\mu\nu}$, $\bar{t}^{\alpha\beta\gamma\delta}$ and their field fluctuations \tilde{u} , $\tilde{s}^{\mu\nu}$, $\tilde{t}^{\alpha\beta\gamma\delta}$ as

* The first two authors contributed equally to the work.

† Corresponding author: lishao@pku.edu.cn

$u = \bar{u} + \tilde{u}$, $s^{\mu\nu} = \bar{s}^{\mu\nu} + \tilde{s}^{\mu\nu}$, $t^{\alpha\beta\gamma\delta} = \bar{t}^{\alpha\beta\gamma\delta} + \tilde{t}^{\alpha\beta\gamma\delta}$. In the weak-field regime and based on a set of reasonable assumptions of the Lorentz-violating fields, it was proved that the vacuum expected value $\bar{s}^{\mu\nu}$ of the field $s^{\mu\nu}$ describes the dominant observable effects [9]. Components of $\bar{s}^{\mu\nu}$ are called the Lorentz-violation coefficients. Extensive experiments have been conducted to constrain the Lorentz-violation coefficients, including laboratory experiments [19, 20], Very Long Baseline Interferometry [21], planetary ephemerides [22], Lunar Laser Ranging (LLR) [23–25], superconducting gravimeters [26], and gravitational waves (GWs) [27–31].

Given the high precision of pulsar observations, pulsars provide an ideal laboratory for test fundamental theories [32–44]. Pulsar timing technology is the common method for processing the times of arrival (TOAs) of radio signals from pulsars. Precision timing of pulses from a pulsar within a binary system provides information about the orbital dynamics of the pulsar [32, 33, 35, 39], which helps us test gravity theories and fundamental principles including the Lorentz symmetry [45–50]. Moreover, recent advancements in pulsar timing array (PTA) research have yielded significant findings [51–55]. Utilizing the network of high-precision pulsars, PTA collaborations reported the evidence of the Hellings-Downs correlation, which is expected from a stochastic GW background. The growing repository of pulsar timing data from PTAs continues to enrich the landscape of scientific inquiry in this field [54, 56–59].

Pulsars also play a critical role in testing Lorentz symmetry [45–50, 60, 61]. Constraints on LV have been imposed from various perspectives through diverse observational phenomena. In the presence of LV, the gravitational dynamics of pulsars is modified since Lorentz-violating terms modify the gravitational field equation [9], which can be manifested as spin precessions of solitary pulsars and orbital dynamics of binary pulsars. The spin precession of pulsars can be studied through the change in profiles of pulses [62–64]. With a circular hollow-cone-like beam model [65], the changes in the pulse profile of PSR B1913+16 are consistent with the prediction of geodetic precession, as a test of GR [62]. Under LV, the spin axis of a pulsar would experience an additional precession around a specific direction since the symmetry of space has been broken [61]. With the non-detection of the changes in pulse profiles of solitary millisecond pulsars, one can obtain tight limits on LV coefficients [45, 61]. For orbital dynamics, through high-precision timing observations of pulsars in binaries, one can obtain measurements of orbital parameters, and thereby constrain LV [45, 46, 48–50]. Moreover, constraints on LV can be derived from alternative observational phenomena beyond pulsar motion, such as the propagation of radiation [29, 66]. LV can lead to energy dependent dispersion relations of photons in vacuum. Through the observation of γ -ray emission up to TeV energies from the Crab pulsar, the MAGIC Collaboration [67] have obtained tight limits in this scenario [68].

In this work we focus on gravitational dynamics with LV. Shao [45] systematically constrained 8 linear combinations of LV coefficients $\bar{s}^{\mu\nu}$ through 27 tests from 13 pulsar systems, including spin precession tests from 2 solitary millisecond pulsars and orbital dynamics tests from 11 binary pulsars. The dimensionless \bar{s}^{Tj} and \bar{s}^{jk} components were constrained to levels of $\mathcal{O}(10^{-9})$ and $\mathcal{O}(10^{-11})$ respectively, where T represents the time coordinate and $j, k = X, Y, Z$ represent the space coordinates in the canonical reference frame for SME. In addition, with the analysis of Lorentz boost effects between different frames, a limit on \bar{s}^{TT} has been obtained from binary pulsars to be smaller than $\mathcal{O}(10^{-5})$ [46]. Because of diverse sky positions and orbital inclinations of binary pulsars, pulsar experiments possess a substantial advantage in breaking the degeneracy between LV coefficients. It is worth noting that the limits on linear combinations of LV coefficients $\bar{s}^{\mu\nu}$ from pulsars in Ref. [45] are global ones, which means that the 8 linear combinations of LV coefficients are constrained simultaneously. Over the last decade, the accumulation of data has enhanced the precision of orbital parameter measurements in binary pulsars, providing a new opportunity to improve the limits on LV. In this paper, we employ a new parameter estimation method and the state-of-the-art pulsar-timing data to constrain the LV coefficients. Compared to the previous limits [45], the precision of the limits has globally been improved by a factor of two to three.

The paper is organized as follows. In Sec. II, we provide a brief overview of the observable effects of pulsars in the context of LV. In Sec. III, we present our parameter estimation method and derive new results of limits on LV coefficients. In Sec. IV, we offer a statistical analysis on methods for improving the limits further and demonstrate through simulations that additional observations of spin precession from solitary millisecond pulsars will significantly enhance the precision of the limits. Section V gives the summary. In this paper, we adopt the units where the light speed $c = 1$.

II. OBSERVABLE EFFECTS OF PULSARS WITH LV

In this section, we overview the observable effects of pulsars with LV [9, 45, 61]. In Sec. II A, We establish the coordinate system and present the transformation of $\bar{s}^{\mu\nu}$ between different Lorentz frames. After that, we introduce the spin precession of solitary pulsars and orbital dynamics of binary pulsars in the presence of LV respectively in Sec. II B and Sec. II C.

A. Coordinate systems

The LV coefficients, $\bar{s}^{\mu\nu}$, are observer Lorentz invariant but particle Lorentz violating [16]. As a result, to probe the magnitudes of $\bar{s}^{\mu\nu}$, it is necessary to explic-

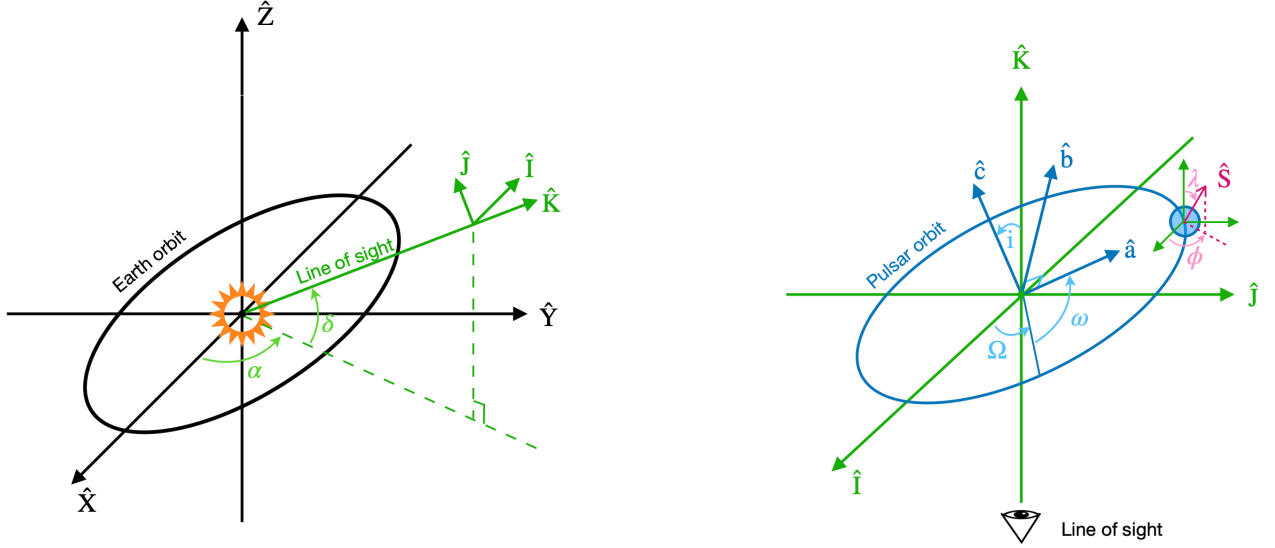


FIG. 1: The Sun-centered celestial-equatorial frame $(\hat{X}, \hat{Y}, \hat{Z})$ is the canonical spatial reference frame for SME. \hat{X} represents the direction from the Earth to the Sun at the vernal equinox, \hat{Z} is along the spin axis of the Earth, and $\hat{Y} \equiv \hat{Z} \times \hat{X}$ [8]. The frame $(\hat{I}, \hat{J}, \hat{K})$ is the comoving frame with the pulsar system. \hat{K} points to the pulsar along the line of sight, and (\hat{I}, \hat{J}) is in the plane of sky with \hat{I} pointing to the east and \hat{J} point to the north [69]. The frames $(\hat{X}, \hat{Y}, \hat{Z})$ and $(\hat{I}, \hat{J}, \hat{K})$ are related by the rotation matrices $\mathcal{R}^{(\alpha)}$ in Eq. (3) and $\mathcal{R}^{(\delta)}$ in Eq. (4) if we ignore the boost between two frames [45]. The frame $(\hat{a}, \hat{b}, \hat{c})$ is the frame related the orbital motion of the binary pulsar. \hat{a} points to the periastron from the center of mass, \hat{c} is along the direction of the orbital momentum, and $\hat{b} \equiv \hat{c} \times \hat{a}$. The frames $(\hat{a}, \hat{b}, \hat{c})$ and $(\hat{X}, \hat{Y}, \hat{Z})$ are related by the rotation matrices $\mathcal{R}^{(\Omega)}$ in Eq. (5), $\mathcal{R}^{(i)}$ in Eq. (6), and $\mathcal{R}^{(\omega)}$ in Eq. (7) [45]. \hat{S} is the spin axis of the pulsar, with a polar angle λ and an azimuthal angle ϕ in the frame $(\hat{I}, \hat{J}, \hat{K})$.

itly specify the observer coordinate system in use. In SME, the standard frame is the Sun-centered celestial-equatorial frame $(T, \hat{X}, \hat{Y}, \hat{Z})$, which is comoving with the Solar system [9]. For a binary pulsar, the most convenient frame $(t, \hat{a}, \hat{b}, \hat{c})$ is defined by its orbit. The two frames are related through a Lorentz transformation [9]. The relative velocity of the pulsar system with respect to the Solar system is on the order of $\mathcal{O}(10^2 \text{ km s}^{-1})$, corresponding to the ratio of the velocity to the speed of light in vacuum on the order of $\mathcal{O}(10^{-3})$. Therefore, in our analysis, we disregard the boost effect and only consider the spatial rotation between two reference frames. The transformation from $(\hat{a}, \hat{b}, \hat{c})$ to $(\hat{X}, \hat{Y}, \hat{Z})$ can be described by a rotation, characterized by right ascension α , declination δ , longitude of ascending node Ω , orbital inclination i , and longitude of periastron ω of the binary pulsar. The frames and related angles are shown in Fig. 1. The full rotation matrix reads [45],

$$\mathcal{R} = \mathcal{R}^{(\omega)} \mathcal{R}^{(i)} \mathcal{R}^{(\Omega)} \mathcal{R}^{(\delta)} \mathcal{R}^{(\alpha)}, \quad (2)$$

where

$$\mathcal{R}^{(\alpha)} = \begin{pmatrix} -\sin \alpha & \cos \alpha & 0 \\ -\cos \alpha & -\sin \alpha & 0 \\ 0 & 0 & 1 \end{pmatrix}, \quad (3)$$

$$\mathcal{R}^{(\delta)} = \begin{pmatrix} 1 & 0 & 0 \\ 0 & \sin \delta & \cos \delta \\ 0 & -\cos \delta & \sin \delta \end{pmatrix}, \quad (4)$$

$$\mathcal{R}^{(\Omega)} = \begin{pmatrix} \cos \Omega & \sin \Omega & 0 \\ -\sin \Omega & \cos \Omega & 0 \\ 0 & 0 & 1 \end{pmatrix}, \quad (5)$$

$$\mathcal{R}^{(i)} = \begin{pmatrix} 1 & 0 & 0 \\ 0 & \cos i & \sin i \\ 0 & -\sin i & \cos i \end{pmatrix}, \quad (6)$$

$$\mathcal{R}^{(\omega)} = \begin{pmatrix} \cos \omega & \sin \omega & 0 \\ -\sin \omega & \cos \omega & 0 \\ 0 & 0 & 1 \end{pmatrix}. \quad (7)$$

For a solitary pulsar, we can set $\mathcal{R}^{(\Omega)}$, $\mathcal{R}^{(i)}$, and $\mathcal{R}^{(\omega)}$ to the unit matrix.

The transformation of $\bar{s}^{\mu\nu}$ are [45]

$$\bar{s}^{tt} \doteq \bar{s}^{Tt}, \quad (8)$$

$$\bar{s}^{tA} \doteq \mathcal{R}_x^A \bar{s}^{Tx}, \quad (9)$$

$$\bar{s}^{AB} \doteq \mathcal{R}_x^A \mathcal{R}_y^B \bar{s}^{xy}, \quad (10)$$

where $A, B = a, b, c$ and $x, y = X, Y, Z$.

B. Spin precession of solitary pulsars

LV destroys the isotropy of space in a manner that a preferred inertial frame is established. In this scenario, a preferred direction emerges, which is determined by the Lorentz-violating fields. In the case of a spinning solitary pulsar, if this preferred direction is misaligned with its spin axis, it disrupts the axial symmetry of the system, leading to spin precession [70]. Consequently, the spin axis of a solitary pulsar would experience an extra precession Ω^{prec} around the preferred direction [9, 61]. The precession rate is

$$\Omega_k^{\text{prec}} = \frac{\pi \bar{s}^{jk} \hat{S}^j}{P}, \quad (11)$$

where P is the spin period of the pulsar, and $\hat{\mathbf{S}}$ is the unit vector of the spin direction. The observational manifestation of spin precession is the change in the angle λ (see Fig. 1), which is the angle between the spin axis direction $\hat{\mathbf{S}}$ and our line of sight $\hat{\mathbf{K}}$ [61]. It results in,

$$\dot{\lambda} = \hat{\mathbf{e}} \cdot \Omega^{\text{prec}} = \frac{\pi \bar{s}^{jk} \hat{S}^j e^k}{P}, \quad (12)$$

where $\hat{\mathbf{e}} \equiv \hat{\mathbf{K}} \times \hat{\mathbf{S}} / |\hat{\mathbf{K}} \times \hat{\mathbf{S}}|$.

Furthermore, we can relate the change in λ to the profile of pulses under assumptions of pulsar emission model. We adopt the cone model for simplicity [65, 71]. Different models only affect the results marginally. In cone model, from the geometry, one has [65, 71]

$$\sin^2\left(\frac{W}{4}\right) = \frac{\sin^2(\rho/2) - \sin^2(\beta/2)}{\sin(\alpha + \beta) \sin \alpha}, \quad (13)$$

where W is the width of the pulse, α is the magnetic inclination angle, $\beta \equiv 180^\circ - \lambda - \alpha$ is the impact angle, and ρ is the semi-angle of the open radiating region. Assuming that the radiation property of the pulsar does not change during the observational span, i.e. $d\alpha/dt = d\rho/dt = 0$, combined with Eq. (12), we get the time derivative of the pulse width caused by LV [61],

$$\frac{dW}{dt} = \frac{2\pi \cot \lambda \cos(W/2) + \cot \alpha}{P \sin(W/2)} \bar{s}^{jk} \hat{S}^j e^k. \quad (14)$$

Taking into account the dependence on the pulsar's spin period in Eq. (14), millisecond pulsars are ideal candidates for probing such LV-induced spin precession [45, 61]. Additionally, millisecond pulsars exhibit stable pulse profiles, enhancing the accuracy of pulse width measurements. Furthermore, selecting isolated millisecond pulsars as targets helps minimize the impact of other spin precession effects in our analysis, such as the geodetic precession in binary systems [61].

C. Orbital dynamics of binary pulsars

With LV, the orbital dynamics of pulsars in binary systems will be modified [9]. Within post-Newtonian

approximation and with the technique of osculating elements, secular changes for orbital parameters after averaging over an orbit have been obtained [9]. The orbital-averaged secular change rates of orbital eccentricity e , longitude of periastron ω , and projected semi-major axis of pulsar orbit x are as follows [9, 45]

$$\left\langle \frac{de}{dt} \right\rangle = n_b F_e \sqrt{1 - e^2} (-e F_e \bar{s}^{ab} + 2\delta X \mathcal{V}_O \bar{s}^{0a}), \quad (15)$$

$$\left\langle \frac{d\omega}{dt} \right\rangle = \frac{3n_b \mathcal{V}_O^2}{1 - e^2} - \frac{n_b F_e \cot i}{\sqrt{1 - e^2}} \times \left(\bar{s}^{ac} \sin \omega + \sqrt{1 - e^2} \bar{s}^{bc} \cos \omega + 2\delta X e \mathcal{V}_O \bar{s}^{0c} \cos \omega \right) + n_b F_e \left(F_e \frac{\bar{s}^{aa} - \bar{s}^{bb}}{2} + \frac{2}{e} \delta X \mathcal{V}_O \bar{s}^{0b} \right), \quad (16)$$

$$\left\langle \frac{dx}{dt} \right\rangle = \frac{1 - \delta X F_e \mathcal{V}_O \cos i}{2 \sqrt{1 - e^2}} \times \left(\bar{s}^{ac} \cos \omega - \sqrt{1 - e^2} \bar{s}^{bc} \sin \omega - 2\delta X e \mathcal{V}_O \bar{s}^{0c} \sin \omega \right). \quad (17)$$

The definitions of n_b , F_e , δX , and \mathcal{V}_O are

$$n_b \equiv \frac{2\pi}{P_b}, \quad (18)$$

$$F_e \equiv \frac{1}{1 + \sqrt{1 - e^2}}, \quad (19)$$

$$\delta X \equiv \frac{m_1 - m_2}{m_1 + m_2}, \quad (20)$$

$$\mathcal{V}_O \equiv [G(m_1 + m_2)n_b]^{1/3}. \quad (21)$$

where P_b is the orbital period, m_1 and m_2 are the pulsar mass and the companion mass respectively.

It is worth noting that such orbital-averaged secular change rates in Eqs. (15–17) is not only the contributions from LV effects, but it also contains GR effects. In Eq. (16), the first term independent with LV coefficients is the contribution to periastron advance from GR.

For small-eccentricity binary pulsars ($e \ll 1$), we consider all terms up to $\mathcal{O}(e^0)$. Above equations reduce to [45],

$$\left\langle \frac{de}{dt} \right\rangle \simeq n_b \delta X \mathcal{V}_O \bar{s}^{0a}, \quad (22)$$

$$\left\langle \frac{d\omega}{dt} \right\rangle \simeq 3n_b \mathcal{V}_O^2 + \frac{n_b}{e} \delta X \mathcal{V}_O \bar{s}^{0b}, \quad (23)$$

$$\left\langle \frac{dx}{dt} \right\rangle \simeq \frac{1 - \delta X}{4} \mathcal{V}_O \cos i (\bar{s}^{ac} \cos \omega - \bar{s}^{bc} \sin \omega) \quad (24)$$

Defining the Laplace-Lagrange parameters $\eta \equiv e \sin \omega$ and $\kappa \equiv e \cos \omega$, with Eq. (22) and Eq. (23), we can get [45]

$$\left\langle \frac{d\eta}{dt} \right\rangle \simeq n_b \delta X \mathcal{V}_O (\bar{s}^{0a} \sin \omega + \bar{s}^{0b} \cos \omega) + 3en_b \mathcal{V}_O^2 \cos \omega, \quad (25)$$

$$\left\langle \frac{d\kappa}{dt} \right\rangle \simeq n_b \delta X \mathcal{V}_O (\bar{s}^{0a} \cos \omega - \bar{s}^{0b} \sin \omega) - 3en_b \mathcal{V}_O^2 \sin \omega. \quad (26)$$

III. PARAMETER ESTIMATION AND RESULTS

In this section, we introduce our parameter estimation method and show the new limits on LV coefficients from updated pulsar timing results. Section III A describes the selected pulsar systems and their roles in constraining LV coefficients. In Sec. III B, we illustrate the parameter estimation method in use and show the results of limits on LV coefficients. We also conduct a brief comparison between our limits and those from GWs [28] and LLR [24].

A. Pulsar systems

We use 12 pulsar systems to constrain the LV coefficients. They can be divided into four classes, (i) solitary pulsars (PSRs B1937+21 and J1744–1134) [61], (ii) small-eccentricity binary pulsars with theory-independent mass measurements (PSRs J1012+5307 [59, 72], J1738+0333 [73], and J0348+0432 [74]), (iii) small-eccentricity binary pulsars without theory-independent mass measurements (PSRs J1713+0747 [52], J0437–4715 [59], J1857+0943 [59], J1909–3744 [75], and J1811–2405 [76]), and (iv) eccentric binary pulsars (PSRs B1534+12 [77] and B2127+11C [78]). Additional descriptions and ephemeris regarding these pulsar systems can be found in Appendix A. As we will see, we construct in total 25 tests from these pulsars.

For solitary pulsars, with non-detection in the change of pulse width, each pulsar system can contribute one constraint according to Eq. (14). The derivative of the pulse width can be measured with dedicated analysis of the pulse profile over long observational spans. The other parameters in Eq. (14) can be obtained from the pulsar timing observations and model fitting to radio and γ -ray lightcurves [61].

For binary pulsars, we have grouped them into three classes according to the eccentricity and whether there are theory-independent mass measurements [45]. Pulsars with theory-independent mass measurements refer to those whose masses are measured based on weak-field Newtonian gravity theory. Three of the small-eccentricity binary pulsars in our samples meet this criterion [72–74]. Their companions are all white dwarfs (WDs), whose masses were measured with well-established WD models through optical observations. Together with pulsar timing observations, we can get the pulsar mass and other orbital parameters. For pulsars with theory-independent mass measurements, each system can provide us with three constraints according to Eqs. (24–26). Pulsars without theory-independent mass measurements refer to those whose masses were measured based on the post-Newtonian effects of GR, such as the Shapiro delay in pulsar timing observation. In modified gravity theories, these post-Newtonian effects would in principle differ from GR, which means the GR-based

mass cannot be trusted with high confidence in tests of modified gravity theories. Considering that $\dot{\omega}$ relates to the periastron advance effects, if we adopt the GR mass, $\dot{\omega}$ tests are not reusable [45], where the overdot notation represents the change rates of parameters. But for \dot{e} and \dot{x} , the gravitational damping contributions can be neglected compared to the measurement accuracy [71]. Therefore, each system can provide two constraints according to Eq. (22) and Eq. (24). For eccentric binary pulsars, there are no theory-independent mass measurements as well. Each system provides two constraints according to Eq. (15) and Eq. (17).

Additionally, following Shao [45] we make the considerations below in our calculations. Firstly, the geometry of some pulsar systems are not fully determined from observations. For solitary pulsars, the azimuthal angle of the spin axis, denoted as ϕ (see Fig. 1), is not observable. For binary pulsars, the longitude of ascending node Ω in some binary pulsars is not determined by pulsar timing. Consequently, we have adopted specific prior distributions for these two parameters and averaged the limits over all potential parameter configurations, which is further explained in Sec. III B. Secondly, it is worth noting that we are calculating *limits* of $\bar{s}^{\mu\nu}$ instead of searching for *signals* of LV. Therefore, we set the observation value related to LV effects to zero, while the measured small deviation from zero is absorbed into the uncertainty. In this case, we are calculating conservative limits of $\bar{s}^{\mu\nu}$. These non-zero deviations can be caused by LV or other systematic errors, and the limits still hold if the non-zero deviations are indeed led by LV. We conservatively estimate 68% confidence level (CL) upper limits for \dot{W} , \dot{e} , \dot{x} , $\dot{\eta}$, and $\dot{\kappa}$ based on the public ephemeris. Taking the estimation for the upper limit of \dot{e} as an example, if the \dot{e} was reported in the ephemeris, i.e. we have known the observed value of \dot{e}_{obs} and the uncertainty $\sigma_{\dot{e}}$, we take the squared sum root of \dot{e}_{obs} and $\sigma_{\dot{e}}$ as a conservative upper limit,

$$|\dot{e}|^{\text{upper}} = \sqrt{\dot{e}_{\text{obs}}^2 + \sigma_{\dot{e}}^2}. \quad (27)$$

If \dot{e} was not reported, we make the upper limit estimation from the uncertainties of e in accordance with the case of linear-in-time evolution [45],

$$|\dot{e}|^{\text{upper}} = \frac{2\sqrt{3}\sigma_e}{T_{\text{obs}}}, \quad (28)$$

where T_{obs} is the observational span. The upper limit estimation of \dot{W} and \dot{x} is the same as that for \dot{e} . It is worth noting that the proper motion of the binary pulsars contributes to \dot{x} , and the observed \dot{x} in some binary pulsars exhibits an offset from zero [79]. We use the upper limit like Eq. (27) for a conservative estimation for \dot{x} caused by LV. For $\dot{\eta}$ and $\dot{\kappa}$, it should be noted that there are terms from GR effects for $\dot{\eta}$ and $\dot{\kappa}$ in Eq. (25) and Eq. (26), so when the LV coefficients are zero, $\dot{\eta}$ and $\dot{\kappa}$ are still not equal to zero. For the sake of parameter estimation simplicity, we absorb these terms into the uncertainties

in a root mean square fashion like Eq. (27), making subsequent treatment consistent with the handling of \dot{W} , \dot{e} , and \dot{x} . In this scenario, we conservatively address the impact of GR effects on our detection of LV-induced periastron advance. Even if LV-induced periastron advance does exist, our conclusions remain valid. These treatments are conservative, and different treatments will not significantly change our results.

B. New limits on LV coefficients

As explained in Sec. III A, the LV coefficients are related to the observable quantities through Eq. (14), Eqs. (15–17), and Eqs. (22–26). Now we construct the parameter-estimation model and explain how we place limits on the LV coefficients. All these relations are linear with respect to the LV coefficients and can be written as

$$\mu_i = D_{i,\alpha} R_{i,\beta}^\alpha M_\gamma^\beta \Theta^\gamma, \quad (29)$$

where μ_i is the predicted values of the observable quantities (such as \dot{e}) when LV occurs. Note that the index i is not summed. $\Theta \equiv \{\Theta^\gamma\}$ is a 8-component vector, which denotes 8 linear combinations of $\bar{s}^{\mu\nu}$. Same as in Ref. [45], we choose the form of 8 linear combinations as

$$\Theta = \left\{ \bar{s}^{\text{TX}}, \bar{s}^{\text{TY}}, \bar{s}^{\text{TZ}}, \bar{s}^{\text{XY}}, \bar{s}^{\text{XZ}}, \bar{s}^{\text{YZ}}, \bar{s}^{\text{XX}} - \bar{s}^{\text{YY}}, \bar{s}^{\text{XX}} + \bar{s}^{\text{YY}} - 2\bar{s}^{\text{ZZ}} \right\}. \quad (30)$$

M_γ^β in Eq. (29) is a 9×8 matrix, which transforms Θ into 9 individual LV coefficients of $\bar{s}^{\mu\nu}$, namely, $\{\bar{s}^{\text{TX}}, \bar{s}^{\text{TY}}, \bar{s}^{\text{TZ}}, \bar{s}^{\text{XY}}, \bar{s}^{\text{XZ}}, \bar{s}^{\text{YZ}}, \bar{s}^{\text{XX}}, \bar{s}^{\text{YY}}, \bar{s}^{\text{ZZ}}\}$ with the condition $\bar{s}^{\text{TT}} = \bar{s}^{\text{XX}} + \bar{s}^{\text{YY}} + \bar{s}^{\text{ZZ}} = 0$ in the Solar system frame. $R_{i,\beta}^\alpha$ is the rotation matrix that transforms $\bar{s}^{\mu\nu}$ from the Solar system frame to the pulsar frame. For different pulsar systems, $R_{i,\beta}^\alpha$ is different. $D_{i,\alpha}$ describes how the LV coefficients in the pulsar frame affect the observable quantities. Finally, we define $L_{i\gamma} \equiv D_{i,\alpha} R_{i,\beta}^\alpha M_\gamma^\beta$, and write the model as

$$\mu = \mathbf{L}\Theta. \quad (31)$$

Note that \mathbf{L} is a 25×8 matrix and depends on unknown angles ϕ and Ω for pulsar systems.

For the i -th observable quantity, we have a central value X_i and a 68% CL bound $|X_i|^{\text{upper}}$. Therefore, in principle one can construct a 68% CL limit for the parameters $|X_i - \mu_i| = |X_i - L_{i\alpha}\Theta^\alpha| \leq |X_i|^{\text{upper}}$. Mathematically, in the 8-d parameter space, this is equivalent to limiting Θ to the region between a pair of 7-d hyperplanes. Combining the 25 pairs of hyperplanes, one obtains a close area in the parameter space.¹ Then calculating the (68% CL) limits of the parameters becomes

¹ Thanks to different sky locations, orbital orientations, and spin axes of different pulsars, the linear-combination coefficients of parameters are linearly independent for different tests. In other words, \mathbf{L} is of column full rank.

a linear programming problem. However, the azimuthal angle ϕ of the spin axis for solitary pulsars, and the longitude of ascending node Ω for some binary pulsars are not observable, which means that one must solve the linear programming problem over all possible configurations of ϕ and Ω . This is not only time-consuming, but also mathematically difficult to define a natural combination for different areas. Shao [45] used Monte Carlo simulations to marginalize over the unknown angles and measurement uncertainties, and only used 8 tightest limits in each simulation. In this work, we improve over the previous method and adopt the Bayesian framework to establish a method that is more statistically sound and yet easier to further extend.

First, we treat the 68% CL bound of the observable quantities as the 1- σ uncertainty σ_i , which is simply $\sigma_i = |X_i|^{\text{upper}}$ for observations with Gaussian noise. Then the likelihood takes a Gaussian form when all ϕ and Ω are fixed,

$$P(\mathbf{X}|\Theta, \xi) \propto \exp \left\{ -\frac{1}{2} [\mathbf{L}\xi\Theta - \mathbf{X}]^\top \mathbf{C}^{-1} [\mathbf{L}\xi\Theta - \mathbf{X}] \right\}, \quad (32)$$

where $\mathbf{C} = \text{diag}\{\sigma_1^2, \sigma_2^2, \dots, \sigma_{25}^2\}$, and ξ denotes the unknown angles. Choosing flat priors, the posterior distribution of Θ given ξ can be analytically calculated as

$$P(\Theta|\mathbf{X}, \xi) \propto \exp \left\{ -\frac{1}{2} [\Theta - \hat{\Theta}_\xi]^\top \mathbf{F}_\xi [\Theta - \hat{\Theta}_\xi] \right\}, \quad (33)$$

where $\hat{\Theta}_\xi = \mathbf{F}_\xi^{-1} \mathbf{L}_\xi^\top \mathbf{C}^{-1} \mathbf{X}$ and $\mathbf{F}_\xi = \mathbf{L}_\xi^\top \mathbf{C}^{-1} \mathbf{L}_\xi$.

Using the formula of total probability, we marginalize over ξ to get the posterior distribution of Θ ,

$$P(\Theta|\mathbf{X}) \propto \int P(\Theta|\mathbf{X}, \xi) p(\xi) d\xi, \quad (34)$$

where $p(\xi)$ is the prior distribution of ξ . For unknown angles ϕ and Ω , we choose the uniform prior $\mathcal{U}(0, 2\pi)$ for each of them.

In practice, $P(\Theta|\mathbf{X}, \xi)$ is a highly non-linear function of ξ , and it is difficult to calculate the integral analytically or numerically. However, for each fixed ξ , the posterior is a simple Gaussian distribution. Since we only need the posterior samples of Θ , we first randomly draw ξ from $p(\xi)$, and generate samples of Θ from the corresponding Gaussian distribution. Finally, we obtain the posterior samples of Θ by putting all the samples together. Compared to Ref. [45], the method here has a more robust statistical explanation by systematically considering the contribution of all limits for every ξ .

In Fig. 2, we show the posterior distribution of Θ . The 1-d marginalized constraints are listed in Table I. Thanks to the utilization of multiple pulsars, there are only small correlations between the LV coefficients. Furthermore, due to the updated, more precise measurements of orbital parameters for binary pulsars, the limits in this work tighten the limits in Ref. [45] by a factor of two to three.

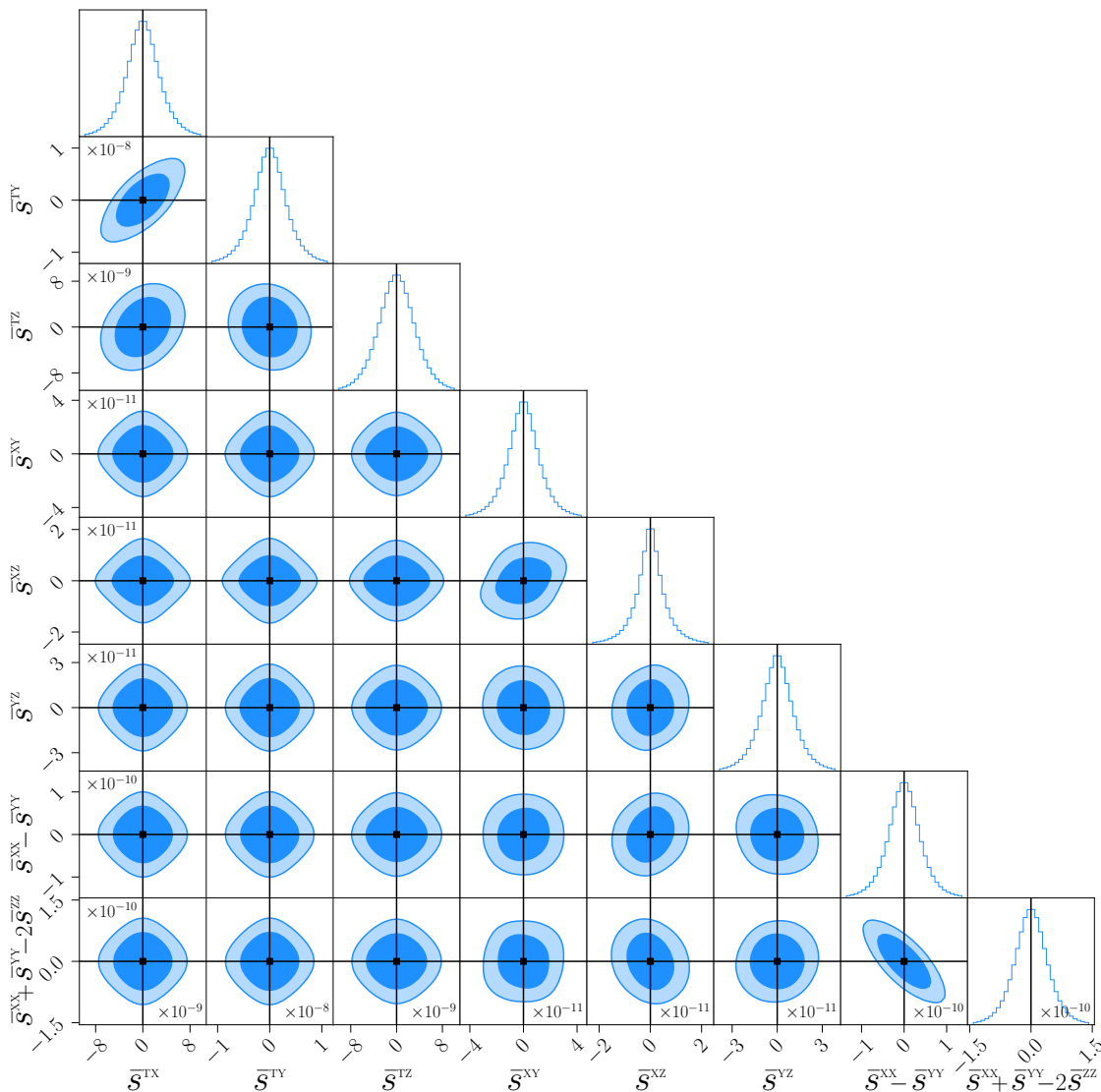


FIG. 2: Global limits on 8 independent linear combinations of LV coefficients, based on 25 tests from 12 pulsar systems. The contours show the 68% and 90% CLs.

Here, we make a brief comparison between our limits and those from GWs [28] and LLR [24]. Based on the observed time delay of $(+1.74 \pm 0.05)$ s between the γ -ray burst, GRB 170817A, and the GW event, GW170817, stringent limits on the LV coefficients have been placed, with upper bounds for s^{Tk} and s^{jk} ($j, k = X, Y, Z$) on the order of $\mathcal{O}(10^{-15})$ to $\mathcal{O}(10^{-14})$ [28]. For limits from the LLR, the upper bounds for s^{Tk} and s^{jk} are on the order of $\mathcal{O}(10^{-9})$ and $\mathcal{O}(10^{-12})$ respectively [24]. It is worth noting that the limits from GWs and LLR are based on the *maximal-reach* method [29, 80, 81], where only one LV coefficient is assumed to be non-zero, and only one observable quantity is used to limit the coefficient. In this paper, the limits on the LV coefficients from pulsars are *global*, which means the correlation between different LV coefficients has been fully taken into

account. Therefore, these approaches are complementary to each other.

IV. PROSPECTS OF LIMITS FROM SPIN PRECESSION OF SOLITARY PULSARS

In this work, the number of observable quantities is larger than the number of free parameters, so the LV coefficients are overly constrained. In order to investigate the contribution of each observable quantity to the final limits, we use the *maximal-reach* method to make order-of-magnitude estimations. We find that the *maximal-reach* results from the binary pulsars are consistent with the global constraints in Sec. III B. Take PSR J1012+5307 as an example, the order-of-magnitude

TABLE I: Global limits on 8 independent linear combinations of LV coefficients based on 25 tests from 12 pulsar systems. The K -factor represents the improvement over the former limits from pulsars [45].

SME coefficients	68% CL limits	K -factor
$ \bar{s}^{\text{TX}} $	2.9×10^{-9}	1.8
$ \bar{s}^{\text{TY}} $	3.3×10^{-9}	2.4
$ \bar{s}^{\text{TZ}} $	3.2×10^{-9}	1.8
$ \bar{s}^{\text{XY}} $	1.2×10^{-11}	2.9
$ \bar{s}^{\text{XZ}} $	5.6×10^{-12}	3.6
$ \bar{s}^{\text{YZ}} $	1.1×10^{-11}	3.0
$ \bar{s}^{\text{XX}} - \bar{s}^{\text{YY}} $	3.9×10^{-11}	2.6
$ \bar{s}^{\text{XX}} + \bar{s}^{\text{YY}} - 2\bar{s}^{\text{ZZ}} $	4.1×10^{-11}	3.0

estimations of limits on \bar{s}^{Tx} and \bar{s}^{xy} ($x, y = \text{X, Y, Z}$) are $\mathcal{O}(10^{-9})$ and $\mathcal{O}(10^{-11})$ respectively, which are consistent with our global constraints. However, the *maximal-reach* limits on the spatial LV coefficients based on the spin precession of solitary pulsars are about 4 order of magnitude tighter than the global constraints, reaching $\mathcal{O}(10^{-15})$.

To explain this, one needs to consider how a degeneracy in constraints forms. Eqs. (32) and (33) are the standard multiple linear regression, and the contours of the posterior in Eq. (33) are 8-d ellipsoids. According to Eq. (14), tight limits from the spin precession means that some linear combinations of the spatial LV coefficients are strongly limited. For example, assume that $X_1 = 0$ is the time derivative of the pulse width of PSR J1937+21, the corresponding limit is $|L_{1\alpha}\Theta^\alpha| \leq \sigma_1$. Since $\sigma_1/L_{1\alpha} \sim 10^{-15}$ is smaller than other limits, the posterior ellipsoids will be very flat in the direction represented by $L_{1\alpha}$ in the parameter space. Projecting these flat ellipsoids onto the corner plots forms degenerate bands. However, the final posterior is obtained by marginalizing over the unknown angle ϕ . Since changing ϕ is equivalent to rotating the degeneracy direction (also the ellipsoidal contours) in the parameter space, the degenerate bands become wider after the “rotation”, and the scale of the final contours are determined by the longer principal axis of the ellipsoids, about $\mathcal{O}(10^{-11})$ in this case. Similar processes also happen for the other pulsar PSR J1744–1134. The constraints from two pulsars do not contribute to the final results in a dominant way.

However, the mechanism described above implies the prospects of constraining the spatial LV coefficients with more high-quality solitary-pulsar observations. Since Eq. (14) only consists of five spatial LV coefficients, the degeneracy (also the “rotation”) only occurs in the 5-d sub-space. If we find five or more solitary pulsars with non-detection of spin precession of similar precision to PSRs B1937+21 and J1744–1134, all linear combinations of the spatial LV coefficients are expected to be

TABLE II: Prospects for global limits on 8 independent linear combinations of LV coefficients with additional tests from three hypothetical solitary pulsars. The K -factor represents the improvement over the former limits from pulsars [45].

SME coefficients	68% CL limits	K -factor
$ \bar{s}^{\text{TX}} $	2.9×10^{-9}	1.8
$ \bar{s}^{\text{TY}} $	3.3×10^{-9}	2.4
$ \bar{s}^{\text{TZ}} $	3.2×10^{-9}	1.8
$ \bar{s}^{\text{XY}} $	5.9×10^{-15}	6.0×10^3
$ \bar{s}^{\text{XZ}} $	2.4×10^{-15}	8.3×10^3
$ \bar{s}^{\text{YZ}} $	4.7×10^{-15}	7.1×10^3
$ \bar{s}^{\text{XX}} - \bar{s}^{\text{YY}} $	1.2×10^{-14}	8.3×10^3
$ \bar{s}^{\text{XX}} + \bar{s}^{\text{YY}} - 2\bar{s}^{\text{ZZ}} $	1.3×10^{-14}	9.6×10^3

limited to the $\mathcal{O}(10^{-15})$ level. In this case, the contours in the 5-d space are ellipsoids with similar lengths on each axis, and the rotation of the ellipsoids will not expand the contours significantly, keeping the constraints still at the $\mathcal{O}(10^{-15})$ level. To verify this, we add three hypothetical solitary pulsars into the ephemeris and calculate the global constraints. The three hypothetical pulsars share the same radiation characteristics as PSR B1937+21, and we assume that the observations provide the same time derivative of pulse width constraints as PSR B1937+21. Unlike PSR B1937+21, their spin periods are set to 5 ms, which is more conservative compared to the spin period of PSR B1937+21 which is 1.56 ms. Additionally, they have different sky locations than PSR B1937+21. We rerun the simulation and the results are shown in Table II. As expected, the limits on the spatial LV coefficients are improved by about 3 to 4 orders of magnitude. We note that there is already a considerable amount of pulsar data available to perform this test. We encourage pulsar observers to consider undertaking such analysis.

V. SUMMARY

In this paper, we calculate the limits on the LV coefficients $\bar{s}^{\mu\nu}$ in the minimal gravity sector based on the latest pulsar observational data. Using twenty-five constraints from twelve pulsar systems, we obtain global limits on eight linear combinations of the LV coefficients. The diverse sky positions of pulsar systems have been instrumental in breaking the degeneracy among LV coefficients. Benefiting from nearly a decade of accumulated pulsar timing data, we tighten the constraints for two to three times compared to the results in Ref. [45].

Based on Bayesian analysis, we have employed a new parameter estimation method that accounts for the randomness introduced by uncertain parameters, such as the longitude of the ascending node in certain binary pul-

sar systems. In addition, we discuss how the constraints from the pulsar systems affect the final global limits on $\bar{s}^{\mu\nu}$. In the case of global constraining, both the quality and quantity of constraints from pulsar systems are of paramount importance. We simulate the precision improvements brought by introducing constraints on spin precession from three hypothetical solitary pulsars, showing that additional observations of solitary pulsar could potentially enhance limits on spatial LV coefficients by three to four orders of magnitude.

As observational data from PTA continues to accumulate, it is anticipated that constraints on LV coefficients from pulsar systems will become increasingly stringent. In the future, the next-generation radio telescopes like the Square Kilometer Array (SKA) and next-generation Very Large Array (ngVLA) will be constructed, providing more precise measurements in observations of pulsars [82, 83]. Pulsars will play an increasingly significant role in Lorentz symmetry tests.

ACKNOWLEDGMENTS

We thank Xueli Miao for useful discussions and the anonymous referee for constructive comments. This work was supported by the National SKA Program of China (2020SKA0120300), the National Natural Science Foundation of China (11975027, 11991053), the Beijing Natural Science Foundation (1242018), the Max Planck Partner Group Program funded by the Max Planck Society, and the High-Performance Computing Platform of Peking University. Y.D. and Z.W. were respectively supported by the National Training Program of Innovation for Undergraduates and the Hui-Chun Chin & Tsung-Dao Lee Chinese Undergraduate Research Endowment (Chun-Tsung Endowment) at Peking University.

Appendix A: Overview of pulsar systems in LV tests

In limiting the pure-gravity sector of minimal SME, 12 pulsar systems are used. They are grouped into four classes, (i) solitary pulsars (PSRs B1937+21 and J1744–1134) [61], (ii) small-eccentricity binary pulsars with theory-independent mass measurements (PSRs J1012+5307 [59, 72], J1738+0333 [73], and J0348+0432 [74]), (iii) small-eccentricity binary pulsars without theory-independent mass measurements (PSRs J1713+0747 [52], J0437–4715 [59], J1857+0943 [59], J1909–3744 [75], and J1811–2405 [76]), and (iv) eccentric binary pulsars (PSRs B1534+12 [77] and B2127+11C [78]). Most of the selected pulsars are consistent with those in Ref. [45], except for the addition of PSRs J1713+0747 and J1811–2405, and the removal of PSRs J1802–2124, B1913+16, and J0737–3039A. Our selection criteria take into account both the precision of constraints and the required properties of pulsar systems. For example,

the double pulsar PSR J0737–3039A’s periastron has rotated by $\sim 270^\circ$ with 16 years of data [39] which makes our linear treatment inappropriate. A better timing model should be designed [84], which is beyond the scope of current paper.

For precision of constraints, we make simple estimations based on Eqs. (14–17) and Eqs. (22–26). For example, Eq. (14) suggests that a large spin rate is beneficial for the final limits on $\bar{s}^{\mu\nu}$ for solitary pulsars. We choose to exclude PSR J1802–2124 [85], which provided relatively loose constraints than the same types of binary pulsars.

For binary pulsars, there are some relevant quantities inferred by us based on the public ephemeris, such as the characteristic velocity of pulsars. Since we cannot ascertain correlations between the observed parameters from publicly available ephemeris, this inference is rough, but suffices for the purpose of this paper.

Solitary pulsars

The relevant quantities used in our limits of solitary pulsars, PSRs B1937+21 and J1744–1134 are shown in Table III [61]. PSR B1937+21 (a.k.a PSR J1939+2134) is the first discovered millisecond pulsar, with a spin period of 1.56 ms. Since its discovery in 1982, it has been observed continuously and frequently and also selected as an important target for PTAs [56]. It is a bright pulsar in the radio band and its profile consists of a main-pulse and an interpulse. PSR J1744–1134 is also a target in PTAs with frequent observations [56–58]. Its spin period is 4.07 ms. This pulsar has a clear main-pulse, and the pulse profile is stable against time. Based on the observations from the 100-m Effelsberg radio telescope covering a time span of approximately 15 years, Shao *et al.* [61] analyzed changes in pulse profiles of PSRs B1937+21 and J1744–1134 and measured the time derivative of pulse width \dot{W} (see Table III). The non-detection of \dot{W} has put a stringent limit on the post-Newtonian parameter $\hat{\alpha}_2$ as $|\hat{\alpha}_2| < 1.6 \times 10^{-9}$ at 95% CL [61].

Small-eccentricity binary pulsars with theory-independent mass measurements

PSRs J1012+5307 [59, 72], J1738+0333 [73], and J0348+0432 [74] have theory-independent mass measurements, whose orbital parameters are shown in Table IV. For binary pulsars, traditional mass measurements are based on the timing analysis. Pulsar mass can be determined when two or more post-Keplerian parameters have been measured, such as the periastron advance and Shapiro delay. However, the pulsar mass inferred from post-Keplerian parameters is already under the presumption of the validity of GR. For a pulsar with a WD companion, multiwavelength observations of a binary system may enable a new path to determine the pulsar mass.

TABLE III: Relevant quantities of PSRs B1937+21 and J1744–1134 for our tests. Most of quantities are from pulsar timing, while the orientation and radiation parameters (α and ζ) are determined through model fitting based on radio and γ -ray lightcurves. The limits on time derivative of the pulse width at 50% intensity are from Ref. [61]. For PSR B1937+21, quantities for the main-pulse (left) and the interpulse (right) are both tabulated. Parenthesized numbers represent the $1\text{-}\sigma$ uncertainty in the last digits quoted.

Pulsar	PSR B1937+21 [61]	PSR J1744–1134 [61]
Discovery year	1982	1997
Right Ascension, α (J2000)	19 ^h 39 ^m 38 ^s .561297(2)	17 ^h 44 ^m 29 ^s .403209(4)
Declination, δ (J2000)	+21°34′59″.12950(4)	−11°34′54″.6606(2)
Spin period, P (ms)	1.55780653910(3)	4.074545940854022(8)
Proper motion in α , μ_α (mas yr ^{−1})	0.072(1)	18.804(8)
Proper motion in δ , μ_δ (mas yr ^{−1})	−0.415(2)	−9.40(3)
Magnetic inclination, α (deg)	75 ⁺⁸ _{−6} / 105 ⁺⁶ _{−8}	51 ⁺¹⁶ _{−19}
Observer angle, $\zeta \equiv 180^\circ - \lambda$ (deg)	80(3)	85 ⁺³ _{−12}
Time span of data (MJD)	50693–55725	50460–55962
Pulse width at 50% intensity, W_{50} (deg)	8.281(9) / 10.245(17)	12.53(3)
Time derivative of W_{50} , \dot{W}_{50} (10 ^{−3} deg yr ^{−1})	−3.2(34) / 3.5(66)	1.3(72)
Estimated Upper Limits		
$ \dot{W}_{50} $ (10 ^{−3} deg yr ^{−1})	4.7 / 7.5	7.3

From the optical spectroscopic observations of the WD companion, WD mass can be inferred based on the well-established WD models. Together with the Keplerian parameters obtained from the timing analysis of the pulsar, pulsar mass can be inferred only under the presumption of the validity of Newtonian gravity. Such mass inference method is not based on GR, and we refer it as theory-independent mass measurements [45].

PSR J1012+5307 is a millisecond pulsar in a 14.5-h orbit with a $0.16 M_\odot$ WD companion [59, 72]. It is monitored for the detection of nanoHertz GWs in PTAs [56, 57]. Based on the optical spectroscopic observations from the Keck telescope, the WD mass has been inferred through the inspection of evolutionary models for extremely low-mass WDs [72]. Together with the radio observations of the pulsar in the second data release of the International PTA (IPTA) [59], we can infer the pulsar mass and other orbital parameters. Besides, the proper motion, the absolute position and the distance for PSR J1012+5307 have been determined by the Very Long Baseline Array in the MSPSR π project [86, 87]. This pulsar was widely used for tests of gravity theories [60, 88–90].

PSR J1738+0333 is a 5.85-ms pulsar discovered in the 20-cm Multi-Beam search for pulsars in intermediate Galactic latitudes of the Parkes 64-m Radio Telescope [91]. It is in a 8.5-h orbit with a $0.18 M_\odot$ WD companion. PSR J1738+0333 is also an object in PTAs [56, 57]. The Helium-core extremely low-mass WD companion is a well-known pulsating WD with at least

three significant periods of variability, providing us an opportunity to constrain the interior structure of this WD [92]. We adopt the pulsar timing results in Ref. [73] and the WD mass inferred from its spectrum in Ref. [93].

PSR J0348+0432 was a well-known massive pulsar discovered by the Green Bank Telescope [94], and the identification of its optical counterpart is conducted in the Sloan Digital Sky Survey archive, which indicated that the optical properties of the counterpart is consistent with a helium core WD [93]. Subsequent phase-resolved spectra observations allowed for the inference of the WD mass as $0.172 \pm 0.003 M_\odot$. Together with the WD radial velocity and the pulsar radial velocity, which were determined by the optical observations of WD and radio observations of the pulsar, the mass of PSR J0348+0432 was determined to be $2.01 \pm 0.04 M_\odot$ [93]. The extreme gravitational fields possessed by PSR J0348+0432 provide an ideal laboratory for testing gravity theories. Besides, this system also plays a significant role in our understanding of the equation of state of neutron stars and in understanding the pulsar-spin evolution [93].

Small-eccentricity binary pulsars without theory-independent mass measurements

PSR J1713+0747 is one of the most brightest millisecond pulsars with a $0.29 M_\odot$ WD companion. It is monitored by PTAs for the detection of nanoHertz GWs [56–58]. Its narrow pulse width and high spin frequency guar-

TABLE IV: Relevant quantities of PSRs J1012+5307 [59, 72], J1738+0333 [73], and J0348+0432 [74] for our tests from pulsar timing and optical observations. Parenthesized numbers represent the $1\text{-}\sigma$ uncertainty in the last digits quoted. There is an ambiguity between i and $180^\circ - i$ from observation, and only the value $i < 90^\circ$ is tabulated.

Pulsar	PSR J1012+5307	PSR J1738+0333	PSR J0348+0432
Observed Quantities			
Observational span, T_{obs} (year)	~ 17 [59, 72]	~ 10 [73]	~ 4 [74]
Right ascension, α (J2000)	10 ^h 12 ^m 33 ^s .437530(6)	17 ^h 38 ^m 53 ^s .9658386(7)	03 ^h 48 ^m 43 ^s .639000(4)
Declination, δ (J2000)	53°07′02″.30019(6)	03°33′10″.86667(3)	04°32′11″.4580(2)
Proper motion in α , μ_α (mas yr ⁻¹)	2.61(1)	7.037(5)	4.04(16)
Proper motion in δ , μ_δ (mas yr ⁻¹)	-25.49(1)	5.073(12)	3.5(6)
Spin period, P (ms)	5.25574910197013(2)	5.850095859775683(5)	39.1226569017806(5)
Orbital period, P_b (day)	0.604672723085(3)	0.3547907398724(13)	0.102424062722(7)
Projected semimajor axis, x (lt-s)	0.58181754(6)	0.343429130(17)	0.14097938(7)
$\eta \equiv e \sin \omega$ (10^{-7})	11(1)	-1.4(11)	19(10)
$\kappa \equiv e \cos \omega$ (10^{-7})	1(1)	3.1(11)	14(10)
Time derivative of x , \dot{x} (10^{-15} ss ⁻¹)	1.9(3)	0.7(5)	...
Mass ratio, $q \equiv m_1/m_2$	10.44(11)	8.1(2)	11.70(13)
Companion mass, m_2 (M_\odot)	0.165(15)	0.181 $^{+0.008}_{-0.007}$	0.172(3)
Pulsar mass, m_1 (M_\odot)	1.72(16)	1.46 $^{+0.06}_{-0.05}$	2.01(4)
$\delta X \equiv (q - 1)/(q + 1)$	0.826(8)	0.780(5)	0.843(2)
Estimated Upper Limits			
$ \dot{x} $ (10^{-15} ss ⁻¹)	1.9	0.9	1.9
$ \dot{\eta} $ (10^{-15} s ⁻¹)	0.65	1.2	27
$ \dot{\kappa} $ (10^{-15} s ⁻¹)	0.65	1.2	27
Derived Quantities Based on GR			
Orbital inclination, i (deg)	50(2)	32.6(10)	40.2(6)
Advance of periastron, $\dot{\omega}$ (deg yr ⁻¹)	0.70(4)	1.57(5)	14.9(2)
Characteristic velocity, \mathcal{V}_O (km s ⁻¹)	311(9)	355(5)	590(4)

antee exceptionally high timing precision, making it an ideal subject for testing fundamental theories [95]. In our tests, we adopt the results of timing analysis of PSR J1713+0747 in the second data release of EPTA [57]. It is worth noting that PSR J1713+0747, as a nearby pulsar in a wide orbit, allows for the measurements of its annual orbital parallax, which provides a way to determine the longitude of ascending node, to be $91.1 \pm 0.5^\circ$ [57].

PSR J0437-4715 is one of the brightest and closest pulsars. It is in a 5.74-d orbit with a $0.2 M_\odot$ WD companion [59]. This pulsar lies in the opposite direction of the Galactic center, where few pulsars have been observed. For this reason, together with its remarkable rotational stability, it is also a significant target for PTAs and has been observed frequently. We adopt the timing results in the second data release of IPTA [59]. Due to the proximity of this pulsar to Earth, its 3-d orbital geometry was completely determined, with a reported longitude of ascending node as $209 \pm 1^\circ$ [59].

PSR J1857+0943 (a.k.a PSR B1855+09) is a millisec-

ond pulsar detected by the Arecibo telescope in 1986. It is in a 12.3-d orbit with a WD companion. This is the first binary pulsar where Shapiro delay has been measured. PSR J1857+0943 is also monitored by the IPTA to detect GWs [56-58]. The updated timing solution is from the second data release of IPTA [59].

PSR J1909-3744 is a millisecond pulsar with spin period of 2.95 ms, and was detected in the Swinburne High Latitude Pulsar Survey with the Parkes 64-m Radio Telescope [96]. After its discovery, it has been regularly observed with Nançay Radio Telescope since 2004, and the timing precision reaches approximately 100 ns. In 2019, Liu *et al.* [75] reported a high-precision timing result of PSR J1909-3744 and provided a detailed discussion of its astrophysical implication. A new limit on the parametrized post-Newtonian parameter has been obtained as $|\hat{\alpha}_1| < 2.1 \times 10^{-5}$ at 95% CL from this pulsar. PSR J1909-3744 is also one of targets in PTAs for the detection of GWs [56-58].

PSR J1811-2405 was discovered by the High Time

TABLE V: Relevant quantities of PSRs J1713+0747 [57], J0437–4715 [59], and J1857+0943 [59] for our tests. Parenthesized numbers represent the 1- σ uncertainty in the last digits quoted. There is an ambiguity between i and $180^\circ - i$ for PSR J1857+0943, and only the value $i < 90^\circ$ is tabulated.

Pulsar	PSR J1713+0747	PSR J0437–4715	PSR J1857+0943
Observed Quantities			
Observational span, T_{obs} (year)	~ 24 [57]	~ 19 [59]	~ 28 [59]
Right ascension, α (J2000)	17 ^h 13 ^m 49 ^s .5331917(3)	04 ^h 37 ^m 15 ^s .9125330(5)	18 ^h 57 ^m 36 ^s .390622(3)
Declination, δ (J2000)	07°47′37″.49258(1)	−47°15′09″.208600(5)	09°43′17″.20712(7)
Proper motion in α , μ_α (mas yr ^{−1})	4.9215(8)	121.443(1)	−2.652(4)
Proper motion in δ , μ_δ (mas yr ^{−1})	−3.920(2)	−71.474(2)	−5.423(6)
Spin period, P (ms)	4.570136598154467(4)	5.75745193918763(3)	5.36210054870076(2)
Orbital period, P_b (day)	67.8251309746(7)	5.7410458(3)	12.32717138213(4)
Projected semimajor axis, x (lt-s)	32.34241947(4)	3.36672001(5)	9.2307805(1)
Eccentricity, e (10^{-5})	7.49405(2)	1.9182(1)	2.167(2)
Longitude of periastron, ω (deg)	176.2000(4)	1.38(2)	276.47(3)
Epoch of periastron, T_0 (MJD)	48741.97387(7)	55316.6954(3)	53619.522(1)
Time derivative of x , \dot{x} (10^{-15} s s ^{−1})	−0.4(2)
Shapiro delay parameter, s	0.9993(1)
Shapiro delay parameter, r (μ s)	1.21(3)
Longitude of ascending node, Ω (deg)	91.1(5)	209(1)	...
Estimated Upper Limits			
$ \dot{e} $ (10^{-17} s ^{−1})	0.09	0.59	7.7
$ \dot{x} $ (10^{-16} s s ^{−1})	1.8	3.0	4.5
Derived Quantities Based on GR			
Pulsar mass, m_1 (M_\odot)	1.37(2)	1.49(6)	1.38(6)
Companion mass, m_2 (M_\odot)	0.296(3)	0.228(6)	0.245(7)
Inclination, i (deg)	71.3(2)	137.51(2)	87.86(15)
Advance of periastron, $\dot{\omega}$ (deg yr ^{−1})	0.000248(3)	0.0155(4)	0.0042(1)
Characteristic velocity, \mathcal{V}_O (km s ^{−1})	61.9(3)	142(2)	108(2)

Resolution Universe Pulsar Survey conducted with the Parkes radio telescope [97]. It is in a 6.3-d orbit with a likely Helium core WD companion. Since its discovery, observations of this pulsar have been consistently conducted using the Effelsberg and Nançay radio telescopes, resulting in a 7-yr timing data span [98]. The first detection of Shapiro delay was reported in Ref. [98]. Kramer *et al.* [76] undertook observations of this pulsar with MeerKAT and obtained a better detection of Shapiro delay, which is shown in Table VI. The measurement of the projected semi-major axis in this system has been conducted with very high precision.

Eccentric binary pulsars

PSR B1534+12 (a.k.a J1537+1155) is the second discovered double neutron star binary. It is in a 10.1-yr

and highly inclined orbit. Fonseca *et al.* [77] updated the timing analysis of the pulsar based on the 22-yr timing data and accounted for the astrophysical processes that affect the TOAs. Five post-Keplerian parameters have been measured, and the timing results are shown in Table VII. Besides, they analyzed the spin precession rate based on the pulse-structure evolution, which is consistent with expectations of GR [77].

PSR B2127+11C is the double neutron star pulsar system in the globular cluster M15. Based on the timing data from 1989 to 2001 with the Arecibo radio telescope, orbital parameters including several post-Keplerian parameters have been obtained [78]; see Table VII. Tests of GR were conducted in the pulsar mass–companion mass diagram based on three post-Keplerian parameters: gravitational redshift γ , periastron advance rate $\dot{\omega}$, and the intrinsic period derivative \dot{P}_{int} . The precision of the test reached approximately 3% level [78].

TABLE VI: Relevant quantities of PSRs J1909–3744 [75] and J1811–2405 [76] for our tests. Parenthesized numbers represent the $1\text{-}\sigma$ uncertainty in the last digits quoted. There is an ambiguity between i and $180^\circ - i$ for PSR J1909–3744, and only the value $i < 90^\circ$ is tabulated.

Pulsar	PSR J1909–3744	PSR J1811–2405
Observed Quantities		
Observational span, T_{obs} (year)	~ 15 [75]	~ 8 [76]
Right ascension, α (J2000)	19 ^h 09 ^m 47 ^s .4335812(6)	18 ^h 11 ^m 19 ^s .85405(3)
Declination, δ (J2000)	$-37^\circ 44' 14''$.51566(2)	$-24^\circ 05' 18''$.41(2)
Proper motion in α , μ_α (mas yr ⁻¹)	$-9.512(1)$	0.6(1)
Proper motion in δ , μ_δ (mas yr ⁻¹)	$-35.782(5)$...
Spin period, P (ms)	2.94710806976663(1)	2.66059327687742005(5)
Orbital period, P_b (day)	1.533449474305(5)	6.27230620515(7)
Projected semimajor axis, x (lt-s)	1.89799111(3)	5.705656754(4)
Eccentricity, e (10^{-6})	0.115(7)	1.18(3)
Longitude of periastron, ω (deg)	156(5)	62(1)
Epoch of periastron, T_0 (MJD)	...	56328.98(2)
Epoch of ascending node, T_{asc} (MJD)	53113.950742009(5)	...
Time derivative of x , \dot{x} (10^{-16} s s ⁻¹)	$-2.61(55)$...
$\eta \equiv e \sin \omega$ (10^{-7})	$-1.05(5)$...
$\kappa \equiv e \cos \omega$ (10^{-7})	0.468(98)	...
Shapiro delay parameter, s	0.998005(65)	...
Shapiro delay parameter, r (μs)	1.029(5)	...
Orthometric amplitude, h_3 (μs),	...	0.70(3)
Orthometric ratio, ς ,	...	0.79(2)
Estimated Upper Limits		
$ \dot{e} $ (10^{-16} s ⁻¹)	0.53	3.9
$ \dot{x} $ (10^{-16} s s ⁻¹)	2.7	0.52
Derived Quantities Based on GR		
Pulsar mass, m_1 (M_\odot)	1.492(14)	$1.8_{-0.3}^{+0.4}$
Companion mass, m_2 (M_\odot)	0.209(1)	$0.29_{-0.03}^{+0.04}$
Inclination, i (deg)	86.38(6)	$103.5_{-1.9}^{+1.5}$
Advance of periastron, $\dot{\omega}$ (deg yr ⁻¹)	0.1391(7)	0.015(2)
Characteristic velocity, \mathcal{V}_O (km s ⁻¹)	220.6(5)	150(10)

- [1] C. M. Will, *Living Rev. Rel.* **9**, 3 (2006), [arXiv:gr-qc/0510072](#).
- [2] C. M. Will, *Living Rev. Rel.* **17**, 4 (2014), [arXiv:1403.7377 \[gr-qc\]](#).
- [3] G. Bertone and D. Hooper, *Rev. Mod. Phys.* **90**, 045002 (2018), [arXiv:1605.04909 \[astro-ph.CO\]](#).
- [4] I. Debono and G. F. Smoot, *Universe* **2**, 23 (2016), [arXiv:1609.09781 \[gr-qc\]](#).
- [5] R. Gambini and J. Pullin, *Phys. Rev. D* **59**, 124021 (1999), [arXiv:gr-qc/9809038](#).
- [6] G. Amelino-Camelia, *Living Rev. Rel.* **16**, 5 (2013), [arXiv:0806.0339 \[gr-qc\]](#).
- [7] V. A. Kostelecky and S. Samuel, *Phys. Rev. D* **40**, 1886 (1989).
- [8] V. A. Kostelecky and M. Mewes, *Phys. Rev. D* **66**, 056005 (2002), [arXiv:hep-ph/0205211](#).
- [9] Q. G. Bailey and V. A. Kostelecky, *Phys. Rev. D* **74**, 045001 (2006), [arXiv:gr-qc/0603030](#).
- [10] V. A. Kostelecky and S. Samuel, *Phys. Rev. D* **39**, 683 (1989).
- [11] V. A. Kostelecký and R. Potting, *Nucl. Phys. B* **359**, 545 (1991).
- [12] T. Jacobson, S. Liberati, and D. Mattingly, *Annals Phys.* **321**, 150 (2006), [arXiv:astro-ph/0505267](#).

TABLE VII: Relevant quantities of PSRs B1534+12 [77] and B2127+11C [78] for our tests. Parenthesized numbers represent the $1\text{-}\sigma$ uncertainty in the last digits quoted. There is an ambiguity between i and $180^\circ - i$, and only the value $i < 90^\circ$ is tabulated.

Pulsar	PSR B1534+12	PSR B2127+11C
Observed Quantities		
Observational span, T_{obs} (year)	~ 22 [77]	~ 12 [78]
Right ascension, α (J2000)	15 ^h 37 ^m 09 ^s 961730(3)	21 ^h 30 ^m 01 ^s 2042(1)
Declination, δ (J2000)	11 [°] 55′55″.43387(6)	12 [°] 10′38″.209(4)
Proper motion in α , μ_α (mas yr ⁻¹)	1.482(7)	-1.3(5)
Proper motion in δ , μ_δ (mas yr ⁻¹)	-25.285(12)	-3.3(10)
Spin period, P (ms)	37.9044411783046(2)	30.52929614864(1)
Orbital period, P_b (day)	0.420737298881(2)	0.33528204828(5)
Projected semimajor axis, x (lt-s)	3.72946417(13)	2.51845(6)
Eccentricity, e	0.27367740(4)	0.681395(2)
Longitude of periastron, ω (deg)	283.306029(10)	345.3069(5)
Epoch of periastron, T_0 (MJD)	52076.827113271(9)	50000.0643452(3)
Advance of periastron, $\dot{\omega}$ (deg yr ⁻¹)	...	4.4644(1)
Einstein delay parameter, γ (ms)	...	4.78(4)
Estimated Upper Limits		
$ \dot{e} $ (10^{-14} s^{-1})	0.02	1.8
$ \dot{x} $ (10^{-14} ss^{-1})	0.065	55
Derived Quantities Based on GR		
Pulsar mass, m_1 (M_\odot)	1.3330(2)	1.358(10)
Companion mass, m_2 (M_\odot)	1.3455(2)	1.354(10)
Inclination, i (deg)	77.15(3)	50.1(4)
Advance of periastron, $\dot{\omega}$ (deg yr ⁻¹)	1.7546(1)	...
Characteristic velocity, \mathcal{V}_O (km s ⁻¹)	394.60(1)	427.426(7)

- [13] V. A. Kostelecky and N. Russell, *Rev. Mod. Phys.* **83**, 11 (2011), [arXiv:0801.0287 \[hep-ph\]](#).
- [14] D. Colladay and V. A. Kostelecky, *Phys. Rev. D* **55**, 6760 (1997), [arXiv:hep-ph/9703464](#).
- [15] D. Colladay and V. A. Kostelecky, *Phys. Rev. D* **58**, 116002 (1998), [arXiv:hep-ph/9809521](#).
- [16] V. A. Kostelecky, *Phys. Rev. D* **69**, 105009 (2004), [arXiv:hep-th/0312310](#).
- [17] V. A. Kostelecky and M. Mewes, *Phys. Rev. D* **80**, 015020 (2009), [arXiv:0905.0031 \[hep-ph\]](#).
- [18] V. A. Kostelecky and Z. Li, *Phys. Rev. D* **99**, 056016 (2019), [arXiv:1812.11672 \[hep-ph\]](#).
- [19] K.-Y. Chung, S.-w. Chiow, S. Herrmann, S. Chu, and H. Muller, *Phys. Rev. D* **80**, 016002 (2009), [arXiv:0905.1929 \[gr-qc\]](#).
- [20] C.-G. Shao *et al.*, *Phys. Rev. Lett.* **117**, 071102 (2016), [arXiv:1607.06095 \[gr-qc\]](#).
- [21] C. Le Poncin-Lafitte, A. Hees, and S. Lambert, *Phys. Rev. D* **94**, 125030 (2016), [arXiv:1604.01663 \[gr-qc\]](#).
- [22] A. Hees, Q. G. Bailey, C. Le Poncin-Lafitte, A. Bourgoïn, A. Rivoldini, B. Lamine, F. Meynadier, C. Guerlin, and P. Wolf, *Phys. Rev. D* **92**, 064049 (2015), [arXiv:1508.03478 \[gr-qc\]](#).
- [23] A. Bourgoïn, A. Hees, S. Bouquillon, C. Le Poncin-Lafitte, G. Francou, and M. C. Angonin, *Phys. Rev. Lett.* **117**, 241301 (2016), [arXiv:1607.00294 \[gr-qc\]](#).
- [24] A. Bourgoïn, C. Le Poncin-Lafitte, A. Hees, S. Bouquillon, G. Francou, and M.-C. Angonin, *Phys. Rev. Lett.* **119**, 201102 (2017), [arXiv:1706.06294 \[gr-qc\]](#).
- [25] A. Bourgoïn *et al.*, *Phys. Rev. D* **103**, 064055 (2021), [arXiv:2011.06641 \[gr-qc\]](#).
- [26] N. A. Flowers, C. Goodge, and J. D. Tasson, *Phys. Rev. Lett.* **119**, 201101 (2017), [arXiv:1612.08495 \[gr-qc\]](#).
- [27] N. Yunes, K. Yagi, and F. Pretorius, *Phys. Rev. D* **94**, 084002 (2016), [arXiv:1603.08955 \[gr-qc\]](#).
- [28] B. P. Abbott *et al.* (LIGO Scientific, Virgo, Fermi-GBM, INTEGRAL), *Astrophys. J. Lett.* **848**, L13 (2017), [arXiv:1710.05834 \[astro-ph.HE\]](#).
- [29] L. Shao, *Phys. Rev. D* **101**, 104019 (2020), [arXiv:2002.01185 \[hep-ph\]](#).
- [30] Z. Wang, L. Shao, and C. Liu, *Astrophys. J.* **921**, 158 (2021), [arXiv:2108.02974 \[gr-qc\]](#).
- [31] L. Haegel, K. O’Neal-Ault, Q. G. Bailey, J. D. Tasson, M. Bloom, and L. Shao, *Phys. Rev. D* **107**, 064031 (2023), [arXiv:2210.04481 \[gr-qc\]](#).
- [32] J. H. Taylor, L. A. Fowler, and P. M. McCulloch, *Nature*

- 277**, 437 (1979).
- [33] J. H. Taylor, *Phil. Trans. A. Math. Phys. Eng. Sci.* **341**, 117 (1992).
- [34] N. Wex and S. Kopeikin, *Astrophys. J.* **514**, 388 (1999), [arXiv:astro-ph/9811052](#).
- [35] M. Kramer *et al.*, *Science* **314**, 97 (2006), [arXiv:astro-ph/0609417](#).
- [36] M. Kramer, *Int. J. Mod. Phys. D* **25**, 1630029 (2016), [arXiv:1606.03843 \[astro-ph.HE\]](#).
- [37] X. Miao, J. Zhao, L. Shao, N. Wex, M. Kramer, and B.-Q. Ma, *Astrophys. J.* **898**, 69 (2020), [arXiv:2006.09652 \[gr-qc\]](#).
- [38] X. Miao, H. Xu, L. Shao, C. Liu, and B.-Q. Ma, *Astrophys. J.* **921**, 114 (2021), [arXiv:2107.05812 \[astro-ph.HE\]](#).
- [39] M. Kramer *et al.*, *Phys. Rev. X* **11**, 041050 (2021), [arXiv:2112.06795 \[astro-ph.HE\]](#).
- [40] L. Shao, *Lect. Notes Phys.* **1017**, 385 (2023), [arXiv:2206.15187 \[gr-qc\]](#).
- [41] L. Shao and K. Yagi, *Sci. Bull.* **67**, 1946 (2022), [arXiv:2209.03351 \[gr-qc\]](#).
- [42] Y. Dong, L. Shao, Z. Hu, X. Miao, and Z. Wang, *JCAP* **11**, 051 (2022), [arXiv:2210.16130 \[astro-ph.HE\]](#).
- [43] Z. Hu, X. Miao, and L. Shao, (2023), [arXiv:2303.17185 \[astro-ph.HE\]](#).
- [44] Y. Dong, Z. Hu, R. Xu, and L. Shao, *Phys. Rev. D* **108**, 104039 (2023), [arXiv:2309.02871 \[gr-qc\]](#).
- [45] L. Shao, *Phys. Rev. Lett.* **112**, 111103 (2014), [arXiv:1402.6452 \[gr-qc\]](#).
- [46] L. Shao, *Phys. Rev. D* **90**, 122009 (2014), [arXiv:1412.2320 \[gr-qc\]](#).
- [47] R. J. Jennings, J. D. Tasson, and S. Yang, *Phys. Rev. D* **92**, 125028 (2015), [arXiv:1510.03798 \[gr-qc\]](#).
- [48] L. Shao and Q. G. Bailey, *Phys. Rev. D* **98**, 084049 (2018), [arXiv:1810.06332 \[gr-qc\]](#).
- [49] L. Shao and Q. G. Bailey, *Phys. Rev. D* **99**, 084017 (2019), [arXiv:1903.11760 \[gr-qc\]](#).
- [50] L. Shao, *Symmetry* **11**, 1098 (2019), [arXiv:1908.10019 \[hep-ph\]](#).
- [51] G. Agazie *et al.* (NANOGrav), *Astrophys. J. Lett.* **951**, L8 (2023), [arXiv:2306.16213 \[astro-ph.HE\]](#).
- [52] J. Antoniadis *et al.* (EPTA), *Astron. Astrophys.* **678**, A50 (2023), [arXiv:2306.16214 \[astro-ph.HE\]](#).
- [53] D. J. Reardon *et al.*, *Astrophys. J. Lett.* **951**, L6 (2023), [arXiv:2306.16215 \[astro-ph.HE\]](#).
- [54] H. Xu *et al.*, *Res. Astron. Astrophys.* **23**, 075024 (2023), [arXiv:2306.16216 \[astro-ph.HE\]](#).
- [55] J. Antoniadis *et al.*, *Mon. Not. Roy. Astron. Soc.* **510**, 4873 (2022), [arXiv:2201.03980 \[astro-ph.HE\]](#).
- [56] G. Agazie *et al.* (NANOGrav), *Astrophys. J. Lett.* **951**, L9 (2023), [arXiv:2306.16217 \[astro-ph.HE\]](#).
- [57] J. Antoniadis *et al.* (EPTA), *Astron. Astrophys.* **678**, A48 (2023), [arXiv:2306.16224 \[astro-ph.HE\]](#).
- [58] A. Zic *et al.*, *Publ. Astron. Soc. Austral.* **40**, e049 (2023), [arXiv:2306.16230 \[astro-ph.HE\]](#).
- [59] B. B. P. Perera *et al.*, *Mon. Not. Roy. Astron. Soc.* **490**, 4666 (2019), [arXiv:1909.04534 \[astro-ph.HE\]](#).
- [60] L. Shao and N. Wex, *Class. Quant. Grav.* **29**, 215018 (2012), [arXiv:1209.4503 \[gr-qc\]](#).
- [61] L. Shao, R. N. Caballero, M. Kramer, N. Wex, D. J. Champion, and A. Jessner, *Class. Quant. Grav.* **30**, 165019 (2013), [arXiv:1307.2552 \[gr-qc\]](#).
- [62] M. Kramer, *Astrophys. J.* **509**, 856 (1998), [arXiv:astro-ph/9808127](#).
- [63] M. Burgay *et al.*, *Astrophys. J. Lett.* **624**, L113 (2005), [arXiv:astro-ph/0502512](#).
- [64] L. Saha and J. Dyks, *Mon. Not. Roy. Astron. Soc.* **467**, 2529 (2017), [arXiv:1701.06374 \[astro-ph.HE\]](#).
- [65] L. Oster and W. Sieber, *Astrophys. J.* **210**, 220 (1976).
- [66] G. Amelino-Camelia, J. R. Ellis, N. E. Mavromatos, D. V. Nanopoulos, and S. Sarkar, *Nature* **393**, 763 (1998), [arXiv:astro-ph/9712103](#).
- [67] J. Albert *et al.* (MAGIC, Other Contributors), *Phys. Lett. B* **668**, 253 (2008), [arXiv:0708.2889 \[astro-ph\]](#).
- [68] M. L. Ahnen *et al.* (MAGIC), *Astrophys. J. Suppl.* **232**, 9 (2017), [arXiv:1709.00346 \[astro-ph.HE\]](#).
- [69] T. Damour and J. H. Taylor, *Phys. Rev. D* **45**, 1840 (1992).
- [70] K. Nordtvedt, *Astrophys. J.* **320**, 871 (1987).
- [71] D. R. Lorimer and M. Kramer, *Handbook of Pulsar Astronomy* (Cambridge University Press, Cambridge, England, 2005).
- [72] D. Mata Sánchez, A. G. Istrate, M. H. van Kerkwijk, R. P. Breton, and D. L. Kaplan, *Mon. Not. Roy. Astron. Soc.* **494**, 4031 (2020), [arXiv:2004.02901 \[astro-ph.HE\]](#).
- [73] P. C. C. Freire, N. Wex, G. Esposito-Farese, J. P. W. Verbiest, M. Bailes, B. A. Jacoby, M. Kramer, I. H. Stairs, J. Antoniadis, and G. H. Janssen, *Mon. Not. Roy. Astron. Soc.* **423**, 3328 (2012), [arXiv:1205.1450 \[astro-ph.GA\]](#).
- [74] J. Antoniadis *et al.*, *Science* **340**, 6131 (2013), [arXiv:1304.6875 \[astro-ph.HE\]](#).
- [75] K. Liu *et al.*, *Mon. Not. Roy. Astron. Soc.* **499**, 2276 (2020), [arXiv:2009.12544 \[astro-ph.HE\]](#).
- [76] M. Kramer *et al.*, *Mon. Not. Roy. Astron. Soc.* **504**, 2094 (2021), [arXiv:2102.05160 \[astro-ph.HE\]](#).
- [77] E. Fonseca, I. H. Stairs, and S. E. Thorsett, *Astrophys. J.* **787**, 82 (2014), [arXiv:1402.4836 \[astro-ph.HE\]](#).
- [78] B. A. Jacoby, P. B. Cameron, F. A. Jenet, S. B. Anderson, R. N. Murty, and S. R. Kulkarni, *Astrophys. J. Lett.* **644**, L113 (2006), [arXiv:astro-ph/0605375](#).
- [79] S. M. Kopeikin, *Astrophys. J. Lett.* **467**, L93 (1996).
- [80] V. A. Kostelecký and M. Mewes, *Phys. Lett. B* **757**, 510 (2016), [arXiv:1602.04782 \[gr-qc\]](#).
- [81] J. D. Tasson, in *8th Meeting on CPT and Lorentz Symmetry* (2020) pp. 13–16, [arXiv:1907.08106 \[hep-ph\]](#).
- [82] L. Shao *et al.*, *PoS AASKA14*, 042 (2015), [arXiv:1501.00058 \[astro-ph.HE\]](#).
- [83] A. Weltman *et al.*, *Publ. Astron. Soc. Austral.* **37**, e002 (2020), [arXiv:1810.02680 \[astro-ph.CO\]](#).
- [84] N. Wex and M. Kramer, *Mon. Not. Roy. Astron. Soc.* **380**, 455 (2007), [arXiv:0706.2382 \[astro-ph\]](#).
- [85] R. D. Ferdman *et al.*, *Astrophys. J.* **711**, 764 (2010), [arXiv:1002.0514 \[astro-ph.SR\]](#).
- [86] H. Ding, A. T. Deller, P. Freire, D. L. Kaplan, T. J. W. Lazio, R. Shannon, and B. Stappers, *Astrophys. J.* **896**, 85 (2020), [Erratum: *Astrophys. J.* 900, 89 (2020)], [arXiv:2004.14668 \[astro-ph.HE\]](#).
- [87] H. Ding *et al.*, *Mon. Not. Roy. Astron. Soc.* **519**, 4982 (2023), [arXiv:2212.06351 \[astro-ph.HE\]](#).
- [88] L. Shao, N. Sennett, A. Buonanno, M. Kramer, and N. Wex, *Phys. Rev. X* **7**, 041025 (2017), [arXiv:1704.07561 \[gr-qc\]](#).
- [89] R. Nair and N. Yunes, *Phys. Rev. D* **101**, 104011 (2020), [arXiv:2002.02030 \[gr-qc\]](#).
- [90] J. Zhao, P. C. C. Freire, M. Kramer, L. Shao, and N. Wex, *Class. Quant. Grav.* **39**, 11LT01 (2022), [arXiv:2201.03771 \[astro-ph.HE\]](#).

- [91] B. A. Jacoby, M. Bailes, S. M. Ord, H. S. Knight, and A. W. Hotan, *Astrophys. J.* **656**, 408 (2007), [arXiv:astro-ph/0609448](#).
- [92] M. Kilic, J. J. Hermes, A. Gianninas, and W. R. Brown, *Mon. Not. Roy. Astron. Soc.* **446**, L26 (2015), [arXiv:1410.4898 \[astro-ph.SR\]](#).
- [93] J. Antoniadis, M. H. van Kerkwijk, D. Koester, P. C. C. Freire, N. Wex, T. M. Tauris, M. Kramer, and C. G. Bassa, *Mon. Not. Roy. Astron. Soc.* **423**, 3316 (2012), [arXiv:1204.3948 \[astro-ph.HE\]](#).
- [94] J. Boyles *et al.*, *Astrophys. J.* **763**, 80 (2013), [arXiv:1209.4293 \[astro-ph.HE\]](#).
- [95] W. W. Zhu *et al.*, *Mon. Not. Roy. Astron. Soc.* **482**, 3249 (2019), [arXiv:1802.09206 \[astro-ph.HE\]](#).
- [96] B. A. Jacoby, M. Bailes, M. H. van Kerkwijk, S. Ord, A. Hotan, S. R. Kulkarni, and S. B. Anderson, *Astrophys. J. Lett.* **599**, L99 (2003), [arXiv:astro-ph/0311415](#).
- [97] M. J. Keith *et al.*, *Mon. Not. Roy. Astron. Soc.* **409**, 619 (2010), [arXiv:1006.5744 \[astro-ph.HE\]](#).
- [98] C. Ng, L. Guillemot, P. C. C. Freire, M. Kramer, D. J. Champion, I. Cognard, G. Theureau, and E. D. Barr, *Mon. Not. Roy. Astron. Soc.* **493**, 1261 (2020), [arXiv:2002.01009 \[astro-ph.HE\]](#).